Int. J. Electrochem. Sci., 14 **(2019)** 3180 – 3203, doi: 10.20964/2019.04.05

International Journal of ELECTROCHEMICAL SCIENCE
www.electrochemsci.org

A Novel Model for Lithium-ion Battery Aging Quantitative Analysis Based on Pseudo Two-Dimension Expressions

Yizhao Gao[1], *Xi Zhang*[1*], *Jun Yang*[1], *Bangjun Guo*[1], *Xuan Zhou*[2]

[1] School of Mechanical Engineering, Shanghai Jiao Tong University, Shanghai, China
[2] Department of Electrical and Computer Engineering, Kettering University, Flint, USA
[*]E-mail: gaoyizhao@sjtu.edu.cn; braver1980@sjtu.edu.cn; dreamyang@sjtu.edu.cn, jasonguob@gmail.com

Received: 30 August 2018 / *Accepted:* 23 January 2019 / *Published:* 10 March 2019

This paper proposes a novel model for lithium-ion battery aging quantitative analysis considering side reactions. The model is integrated with the transfer function type derived from a pseudo two-dimensional (P2D) model. The capacity fade, solid electrolyte interphase (SEI) growth and deposited layer growth led by the side reactions are selected as degradation representatives. The quantitative relationship between the Li ion concentration and fore-mentioned degradation parameters is established using some mathematical methods e.g., the Laplace transform and the Pade approximation, etc. to somehow indicate the battery aging mechanism. To observe the battery aging, scanning electron microscopy (SEM) and transmission electron microscopy (TEM) were employed to quantify the deposited layer and SEI thickness, respectively. The simulated and experimental results verified the correctness and validity of the proposed model.

Keywords: Lithium-ion battery, Side reaction, SEI growth.

1. INTRODUCTION

Lithium-ion batteries have been commonly regarded as mainstream energy storage components in electric vehicles because of their high energy and power density, long lifespan, and better eco-friendly nature [1-2]. However, battery aging problems (e.g. capacity fade and power fade) are inevitable in the recycling process, and these phenomena become more severe during the charge process. Recent studies have shown that the side reactions are the major factor for lithium-ion battery degradation [3-7]. The side reactions mainly occur at anode surface during charging, consuming Li ions [8]. The low potential difference between electrode and electrolyte at the anode is inductive to side reactions. When battery is charged, the potential across the anode and electrolyte is below 0.5 V, a reduction reaction occurs between the electrolyte and Li^+ [9-10]. The reaction products stick to the surface of the anode particles to form an initial thin film called solid electrolyte interphase (SEI), mainly composed of Li_2CO_3 and

$(CH_2OCH_2Li)_2$ [11]. The products continue to accumulate as the battery is working, leading to a thicker SEI. Due to poor ionic conductivity of the deposit, the overgrowth of SEI film increases internal resistance and power fade [12-15]. In order to study methodologies that could prolong the cycle life and maximize the capability of power cells, a proper degradation mechanism model considering side reactions is necessary for aging process comprehension.

Matilda et al. examined the impact of morphological changes in an aged battery after opening it[1][16]. The results showed that both cycled cells displayed uneven aging within the cell electrodes associated with different SEI characteristics. Agubra et al. found that the rate of side reactions could be increased by raising the SOC range [17]. However, they did not provide corresponding mathematical models to demonstrate these side effects. Doyle et al. investigated the side reactions using the Tafel equation, but no corresponding experiment was carried out to validate the proposed theory [18]. Tanvir et al. proposed a nonlinear, electrolyte-enhanced, single particle model that includes aging due to SEI growth [19]. Fu et al. investigated the mechanism of capacity fade and resistance increase due to side reactions and developed a thermal-electrochemical model for lithium ion batteries [8,10]. Similar physics-based models revealing the effects of side reactions on SEI growth and cell capacity fade could also be found in Ref [20-22]. Nevertheless, most models are basically full order and highly nonlinear. In addition, verification experiments exploring performance degradation were conducted in macroscopic scale and failed to observe the morphology of SEI. A comprehensive verifying experiment scheme including SEI component analysis is insufficient.

In this paper, a novel model for Lithium-ion battery electrochemical aging analysis is proposed which considers side reactions as the main aging factor. Capacity fade caused by side reactions, growth of deposited layer and growth of SEI are selected as degradation representatives to quantify the degradation degree. The mathematical relationship between these degradation representatives and input current is established to form an aging model based on the transfer function type of the simplified P2D electrochemical model. Cycling tests are carried out to validate the model. The aged electrode properties are investigated on several positions in the jellyroll using a combination of microscopic observation tools (SEM & TEM for deposited layer and SEI-, respectively) and component analysis methods of side reaction products (XPS, XRD and EIS) to obtain an overall degradation rule under different charge C-rates. Furthermore, the model is simulated with Simulink and COMSOL. The simulated and experimental results verify the correctness and validity of the proposed model.

The remainder of this paper is listed below. In section 2, the electrochemical aging model is established. In sections 3 and 4, experimental methods and results are analyzed in detail, respectively. In section 5, simulation results and experimental results are compared to validate the model. The conclusion is drawn in section 6.

2. MODEL ESTABLISHMENT

2.1. Transfer-function type P2D model

As shown in Fig.1, the Li-ion battery is composed of two porous electrodes containing many uniform particles and the separator. They are mixed with the electrolyte. the Li ions are de-intercalated from or intercalated to the electrode and migrated through the electrolyte. The particle radius is denoted as *R*. The potentials or concentrations are related to the *x* position and time while the ambient temperature is assumed to be constant.

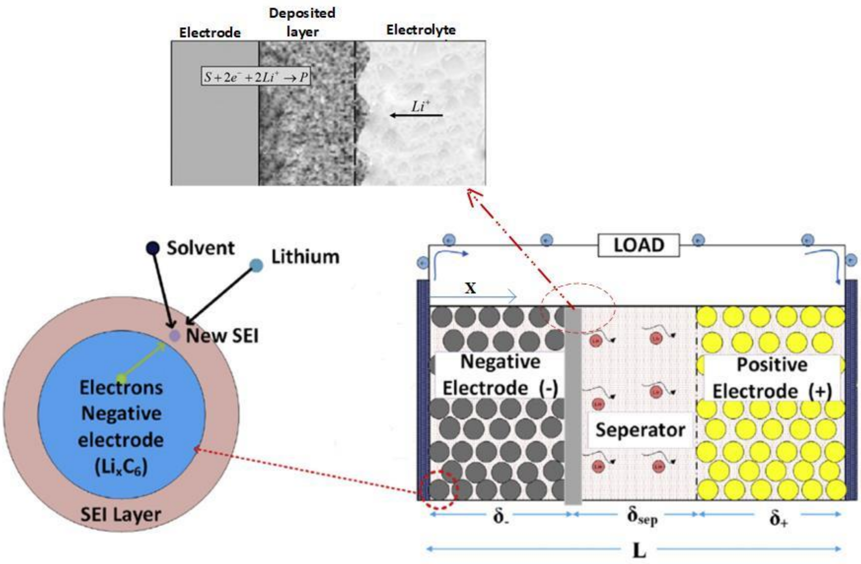

Figure 1. Schematic diagram of the lithium-ion battery.

The fundamental governing equations of a Li-ion cell are listed in Table 1. The Laplace transform, inverse Laplace transform and Pade approximation have been used to obtain a transfer-function-style expression between output voltage and input current. The detailed derivation process can be referred to our aforementioned work [23-25]. The results are summarized in Table 1:

Table 1. P2D transfer-function electrochemical model [23].

Name	Governing Equation	Boundary conditions	Number
Conservation of species in solid phase	$\frac{\partial c_s}{\partial t}=\frac{D_s}{r^2}\frac{\partial}{\partial r}(r^2\frac{\partial c_s}{\partial r})$	$\left.\frac{\partial c_s}{\partial r}\right\|_{r=0}=0, D_s\left.\frac{\partial c_s}{\partial r}\right\|_{r=R_s}=-\frac{j}{F}$	(1)
Conservation of species in electrolyte	$\varepsilon_e\frac{\partial c_e}{\partial t}=D_e^{eff}\frac{\partial^2 c_e}{\partial x^2}+\frac{a_s\left(1-t_+^0\right)}{F}j$	$\left.\frac{\partial c_e}{\partial x}\right\|_{x=0}=\left.\frac{\partial c_e}{\partial x}\right\|_{x=L}=0$	(2)
Conservation of charge in electrodes	$\sigma^{eff}\frac{\partial^2\phi_s}{\partial x^2}-a_S j=0$	$-\sigma_-^{eff}\left.\frac{\partial\phi_s}{\partial x}\right\|_{x=0}=\sigma_+^{eff}\left.\frac{\partial\phi_s}{\partial x}\right\|_{x=L}=\frac{I}{A}$ $\left.\frac{\partial\phi_s}{\partial x}\right\|_{x=\delta_-}=\left.\frac{\partial\phi_s}{\partial x}\right\|_{x=\delta_-+\delta_{sep}}=0$	(3)

Conservation of charge in electrolyte	$k^{eff}\dfrac{\partial^2\phi_e}{\partial x^2}+k_d^{eff}\dfrac{\partial^2\ln c_e}{\partial x^2}+a_s j=0$	$\left.\dfrac{\partial\phi_e}{\partial x}\right\vert_{x=0}=\left.\dfrac{\partial\phi_e}{\partial x}\right\vert_{x=L}=0,$ $\left.\left(k^{eff}\dfrac{\partial\phi_e}{\partial x}+k_d^{eff}\dfrac{\partial c_e}{\partial x}\right)\right\vert_{x_-}$ $=\left.\left(k^{eff}\dfrac{\partial\phi_e}{\partial x}+k_d^{eff}\dfrac{\partial c_e}{\partial x}\right)\right\vert_{x_+}$	(4)
Reaction kinetics	$j=i_0\left(\exp\left(\dfrac{\alpha_a F}{RT}\eta\right)-\exp\left(-\dfrac{\alpha_c F}{RT}\eta\right)\right)$ $\eta=\phi_s-\phi_e-U$		(5)
Pade approximation of transfer function of solid concentration with respect to input current	Positive(x=L) $\dfrac{C_s(s)}{J(s)}=\dfrac{\dfrac{3}{R_s}+\dfrac{2R_s}{7D_s}s}{a_s F(1+\dfrac{1}{35}\dfrac{R_s^2}{D_s}s)s}$	Negative (x=0) $\dfrac{C_s(s)}{J(s)}=-\dfrac{\dfrac{3}{R_s}+\dfrac{2R_s}{7D_s}s}{a_s F(1+\dfrac{1}{35}\dfrac{R_s^2}{D_s}s)s}$	(6)
Pade approximation of transfer function of electrolyte concentration with respect to input current	Positive (x=L) $\dfrac{C_e(s)}{J(s)}=\dfrac{1-t_+^0}{F}\dfrac{0.1406\dfrac{L}{D_e}}{1+0.1173\dfrac{L^2}{D_e}\varepsilon_{e,p}s}$	Negative (x=0) $\dfrac{C_e(s)}{J(s)}=\dfrac{1-t_+^0}{F}\dfrac{0.0862\dfrac{L}{D_e}}{1+0.0752\dfrac{L^2}{D_e}\varepsilon_{e,n}s}$	(7)
Transfer function of overpotential with respect to input current	$\dfrac{\eta(s)}{J(s)}=\dfrac{RT}{Fi_0(\alpha_a+\alpha_c)}$		(8)
Pade approximation of transfer function of electrolyte potential	$\dfrac{\tilde{\Phi}_e(L,s)}{J_p^n(s)}-\dfrac{\tilde{\Phi}_e(0,s)}{J_n^n(s)}=\dfrac{2RT(1-t_+^0)}{c_{e,0}F}\left(\dfrac{C_e(L,s)}{J_p^n(s)}-\dfrac{C_e(0,s)}{J_n^n(s)}\right)$		(9)

with respect to input current		
Resistance voltage drop	$V_f(s)=R_fI(s)$	(10)
Terminal voltage	$V_{cell}(s)=\left(U_p\left(\frac{C_{s,pos}(s)}{C_{s,p,\max}}\right)-U_n\left(\frac{C_{s,neg}(s)}{C_{s,n,\max}}\right)\right)$ $+\left(\eta_p(s)-\eta_n(s)\right)+\left(\tilde{\Phi}_e(L,s)-\tilde{\Phi}_e(0,s)\right)-R_fI(s)$	(11)

r = radial coordinate, c_s=concentration of electrode, D_s= diffusion coefficient of the solid phase, j =particle surface reaction flux, F= Faraday constant (96487C/mol), ε_e =electrolyte volume fraction, D_e = effective electrolyte diffusion coefficient, a_s =specific interfacial surface area, t_+^0 = li-ion transference number, κ = ionic conductivity, κ^{eff} = effective ionic conductivity, κ_d^{eff} =effective diffusion ionic conductivity, $\alpha_{a/c}$ = transfer coefficients, i_0= exchange current density, U=equilibrium potential.

2.2. Electrochemical aging process considering side reactions

The Li ion intercalation current density is represented as j_{int} in Eq. (12a). When side reactions take place at the interface between the electrode particles and the electrolyte, the SEI growth is indicated by Eq. (12b) [5-6].

$$C_6+Li^+ + e^- \longrightarrow LiC_6 \tag{12.a}$$

$$C_2H_4CO_3+2Li^+ + 2e^- \longrightarrow (CH_2OCO_2Li)_2\downarrow +C_2H_4 \tag{12.b}$$

The side reactions current density is denoted as j_{side}. In addition, the total volumetric current density j_{total} is the sum of the current of the above two reactions:

$$j_{total} = j_{\text{int}} + j_{side} \tag{13}$$

The Bulter-Volmer equation in Eq.5 is linearized as:

$$j_{\text{int}} = a_s i_{0,\text{int}} \frac{F(\alpha_{a,\text{int}}+\alpha_{c,\text{int}})}{RT}\eta_{\text{int}} \tag{14}$$

where $i_{0,\text{int}}$ is the exchange current density of lithium intercalation, and η_{int} is the surface overpotential [10]. The η_{int} is defined as:

$$\eta_{\text{int}} = \phi_s - \phi_e - U_{\text{int}} - R_{SEI}\, j_{total} \tag{15}$$

where ϕ_s and ϕ_e are potentials in the solid phase and electrolyte phase, respectively; R_{SEI} is the resistance of the surface film, determined by SEI only; U_{int} is the equilibrium potential for intercalation reaction, according to Nernst Equation, described as:

$$\begin{aligned} U_{\text{int}-} &= U_{\text{int}-}^{\theta}(x) + \frac{RT}{nF} In(\frac{c_{e-}}{c_{e0}}) \\ U_{\text{int}+} &= U_{\text{int}+}^{\theta}(\text{y}) + \frac{RT}{nF} In(\frac{c_{e+}}{c_{e0}}) \end{aligned} \tag{16}$$

Where $U^{\theta}_{\text{int}+}(\text{y})$ and $U^{\theta}_{\text{int}-}(x)$ are the standard equilibrium potentials. Open circuit voltage (OCV) is equal to the difference between the two equilibrium potentials on the cathode and anode;

$$OCV = U^{\theta}_{\text{int}+}(\text{y}) - U^{\theta}_{\text{int}-}(x) \tag{17}$$

The current density of side reactions is governed by the Tafel formula as follows:

$$j_{side} = \text{-i}_{0,side}\exp\left(-\frac{\alpha_{c,side} n_{side} F}{RT}\eta_{side}\right) \tag{18}$$

where $\text{i}_{0,side}$ is the exchange current density of side reactions and n_{side} is the number of ions involved in the side reactions which is equal to 2 in this study [8]. Overpotential of side reactions, η_{side} ,is described as:

$$\eta_{\text{side}} = \phi_s - \phi_e - U_{eq,side} - R_{SEI}\, j_{total} \tag{19}$$

where $U_{eq,side}$ is the equilibrium potential of the side reactions:

$$U_{eq,side} = U^{\theta}_{eq,side} + \frac{RT}{n_{side}F} In\left(\frac{c_e}{c_{e0}}\right) \tag{20}$$

$U^{\theta}_{eq,side}$ is assumed to be a constant and equals to 0.21V in this paper. Combing Eqs. (15), (17), (19) and (20), another form of η_{side} is deduced below:

$$\eta_{side} = \eta_{-} + \frac{RT}{2F} In\left(\frac{c_{e-}}{c_{e0}}\right) + U^{\theta}_{\text{int}-}(x) - U^{\theta}_{eq,side} \tag{21}$$

The capacity fade caused by side reaction Q_{side} is defined as the integration of the side reaction rate, j_{side} over the volume of composite anode with time:

$$Q_{side}(\tau) = \text{-}\int_{x=0}^{\delta_{-}}\left(\int_{t=0}^{\tau} j_{side}(x,t)\, a_s\, dt\right) A dx \tag{22}$$

where the unit of Q_{side} is Ah, δ_{-} denotes the thickness of composite anode (m), τ is the total operating time (s), A is the electrode plate area, and a_s is active surface area per electrode unit volume [19].

The volume fraction of SEI, ε_{SEI} , is defined as:

$$\Delta\varepsilon_{SEI}(\tau, x) = \frac{\overset{\square}{V}_{SEI}}{n_{side}F}\int_{t=0}^{\tau} j_{side}(x,t)\, a_s\, dt \tag{23}$$

$\overset{\square}{V}_{SEI}$ denotes the molar volume of SEI. Then the resistance and thickness of SEI can be expressed as:

$$\begin{aligned} R_{SEI}(\tau, x) &= \frac{\Delta\varepsilon_{SEI}(\tau, x)}{k_{SEI}} \\ \delta_{SEI}(\tau, x) &= \frac{\Delta\varepsilon_{SEI}(\tau, x)}{a_s} \end{aligned} \tag{24}$$

where k_{SEI} is the ionic conductivity of SEI. Considering the anode particles are glued together by binders, the growth of SEI is mechanically resistive. In contrast, the deposited layer (DL) is much thicker than SEI. The region of deposited layer formation is $\delta_{-} - R_s < x < \delta_{-}$, where R_s denotes the radius of active particles close to the separator [26]. The growth of deposited layer can be obtained as:

$$\delta_{DL}(\tau) = \frac{\overset{\square}{V}_{DL}\, R_s}{n_{side}F} \int_{t=0}^{\tau} j_{side}(\delta_{-}, t) a_s dt \qquad (25)$$

2.3. Derivation of aging model

Capacity fade Q_{side}, SEI growth δ_{SEI}, and deposited layer growth δ_{DL}, are adopted as degradation representatives. The main objective is to obtain the expression of the degradation parameters versus various input currents. The Taylor expansion can be applied to Eq. (21) to obtain a linearized expression of η_{side} below:

$$\eta_{side} = \eta_{-} + \frac{RT}{2F}\frac{c_{e-}}{c_{e0}} + U^{\theta}_{\text{int}-}(x) - U^{\theta}_{eq,side} - \frac{RT}{2F} \qquad (26)$$

Then the Laplace transform is used for Eq. (26) transformation, considering the transfer-function type of $\frac{C_e(s)}{J(s)}$ in Eq. (7) and $\frac{\eta(s)}{J(s)}$ in Eq. (8). Consequently, the relationship of the overpotential of the side reactions and the current density can be given by:

$$\lambda(s) = \frac{\eta_{side}(s)}{J(s)} = \frac{RT}{a_s i_0 F(\alpha_a + \alpha_c)} + \frac{RT}{2F^2 c_{e0}}\frac{1-t_+^0}{F}\frac{0.0862\frac{L^2}{D_e}}{1+0.0752\frac{L^2}{D_e}\varepsilon_{e,n}s} + \frac{L(U^{\theta}_{\text{int}-})}{J(s)} - \frac{L(U^{\theta}_{eq,side})}{J(s)} - \frac{L(\frac{RT}{2F})}{J(s)} \qquad (27)$$

where L() means the Laplace transform, and $U^{\theta}_{\text{int}-}(x)$ can be obtained through a set of data provided by the manufacturer. $U^{\theta}_{eq,side}$ and $\frac{RT}{2F}$ are constants. Thus, the last three terms can be treated as known quantities. Furthermore, when the input current density J is given, η_{side}, can be calculated based on Eq. (27).

Eq. (18) is linearized as:

$$j_{side} = \frac{\mathrm{i}_{0,side}\alpha_{c,side}n_{side}F}{RT}\eta_{side} \qquad (28)$$

Combined with Eq. (27), $\frac{j_{side}(s)}{J(s)}$ is expressed as:

$$\frac{j_{side}(s)}{J(s)} = \frac{\mathrm{i}_{0,side}\alpha_{c,side}n_{side}F}{RT}\lambda(s) \qquad (29)$$

Furthermore, the integral order of Eq. (22) is switched and Laplace transform is applied, then $\frac{Q_{side}(s)}{J(s)}$ is deduced as:

$$\frac{Q_{side}(s)}{J(s)} = -A\int_{x=0}^{\delta_n} \frac{j^{Li}_{side}(x,s)}{sJ(s)} = -\frac{A\mathrm{i}_{0,side}\alpha_{c,side}n_{side}F}{RT}\int_{x=0}^{\delta_n}\frac{\lambda(s)}{s}dx \qquad (30)$$

δ_{SEI} and δ_{DL} are expressed as:

$$\frac{\delta_{SEI}(s)}{J(s)} = \frac{\bar{V}_{SEI}}{2Fa_s}\frac{j_{side}^{Li}(x,s)}{s}$$
$$\frac{\delta_{DL}(s)}{J(s)} = \frac{\bar{V}_{DL}R_S}{2F}\frac{j_{side}^{Li}(\delta_-,s)}{s} \qquad (31)$$

Based on Eq.30 and Eq.31, the mathematical transfer-function relationship between current and three aging parameters Q_{side}, δ_{SEI}, δ_{DL} are obtained. For better analysis, the block diagram of the electrochemical aging model integrated with those relationships is illustrated in Fig.2. The electrochemical parameters involved in this paper is summarized in Table 2.

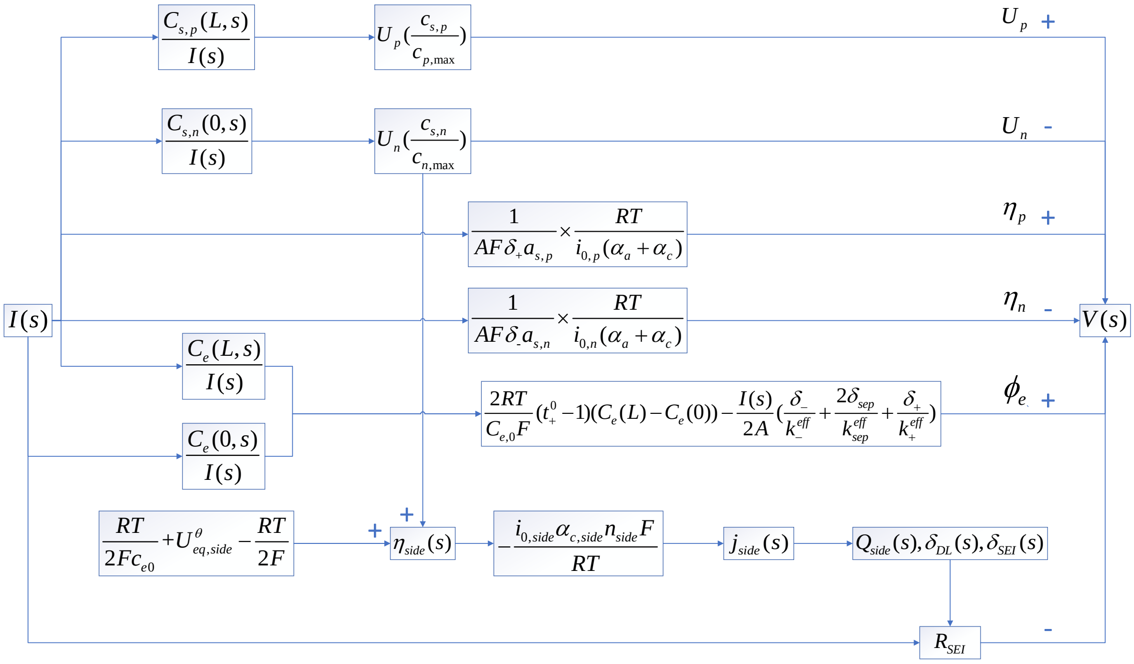

Figure 2. Block diagram of the electrochemical aging model.

To validate the effectiveness of the proposed simplified transfer-function type aging model, we simulated it in the MATLAB using the Laptop compared with the full-order model. The computation time for both models were summarized in Table 3. The input of these two models is 1C, 2C, 3C and 4C constant current constant voltage (CCCV) charging curve in one cycle.

Table 3. Simulation time for two kinds of battery aging models

	1C	2C	3C	4C
Full-order model	4.8 s	4.3 s	4.2 s	4.1 s
Simplified aging model	1.9 s	1.7 s	1.5 s	1.4 s

As can be seen from Table 3, the simulation time for the simplified model introduced in the section 2.3 is able to reduce the calculation time significantly compared to the full model in the section 2.2. As for the model precision, we will introduce it in the section 5.

Table 2. Electrochemical parameters of the 18650 NCM battery

Symbol	Units	Negative	Separator	Positive
D_s	m^2s^{-1}	2.7×10^{-16}		3×10^{-16}
D_e	m^2s^{-1}	4.27×10^{-11}	9.19×10^{-11}	4.2×10^{-11}
L	m	39.5×10^{-6}	25×10^{-6}	36.55×10^{-6}
R	m	10.9×10^{-6}		10.9×10^{-6}
A	m^2	0.155	0.155	0.155
κ	$S\ m^{-1}$	0.1040	0.2238	0.1040
ε_s		0.595		0.63
ε_e		0.3	0.5	0.3
t_+^0		0.363	0.363	0.363
$C_{s,\ max}$	$mol\ m^{-3}$	30.6×10^3		51.6×10^{-3}
$C_{s,0}$	$mol\ m^{-3}$	25.48×10^3		18.64×10^3
$C_{e,0}$	$mol\ m^{-3}$	1200	1200	1200
α		0.5		0.5
Stoichiometry at 0% SOC		0.03		0.95
Stoichiometry at 100% SOC		0.81		0.35
V_{SEI}[a]	m^3mol^{-1}	2×10^{-6}		
V_{DL}[b]	m^3mol^{-1}	34.76		
$U_{eq,side}^{\theta}$[a]		0.21		
κ_{SEI}[c]	$S\ m^{-1}$	1×10^{-2}		
$i_{0,side}$[c]	Am^{-2}	1.5×10^{-8}		
$\alpha_{c,side}$[a]		0.7		
n_{side}[a]		2		

[a]Rujian Fu et al [8]

[b]optimized by comparing simulation to the thickness of DL measured by SEM

[c]T.R.Ashwin et al[27]

3. DESIGN OF EXPERIMENTAL SCHEMES

The lithium-ion cells used in this study are the commercial LG-MG1 18650 NCM cylindrical cells with 2.6 Ah nominal capacity. The cathode active material is $Li[MnNiCo]O_2$ and anode material is made of carbon with polyvinylidene fluoride (PVDF) as the binding material. The current collectors for anode and cathode electrodes are copper and aluminum, respectively. The battery has a polymer electrolyte that consists of polyethylene oxide with lithium salt, $LiPF_6$, with co-solvents of ethylene carbonate (EC), and dimethyl carbonate (DMC).

3.1. Cycling aging of commercial cells

The cells are divided into four groups and then put into cycling test using the cell tester and a temperature-controlled chamber at constant ambient temperature, 25 °C. Four groups correspond to four different aging conditions. The charge current for each group varies, referred to as 1C, 2C, 3C and 4C respectively. The discharge current is 3C for each group. In every cycle, the cell is charged by a constant current (CC) step to a cut-off voltage of 4.2V, followed by a constant voltage (CV) step at 4.2V until the charge current drops below 0.15A. After 10 min, the cell is discharged at a constant current of 3C to 2.5V, followed by another 10 min rest before moving to the next cycle. Periodically, the cell is taken to the capacity test (1C CCCV) every 20 cycles. After cycling completes, the cycled cells are sent to the EIS test station for their impedance spectra measurement.

3.2. Morphology and structure characterization

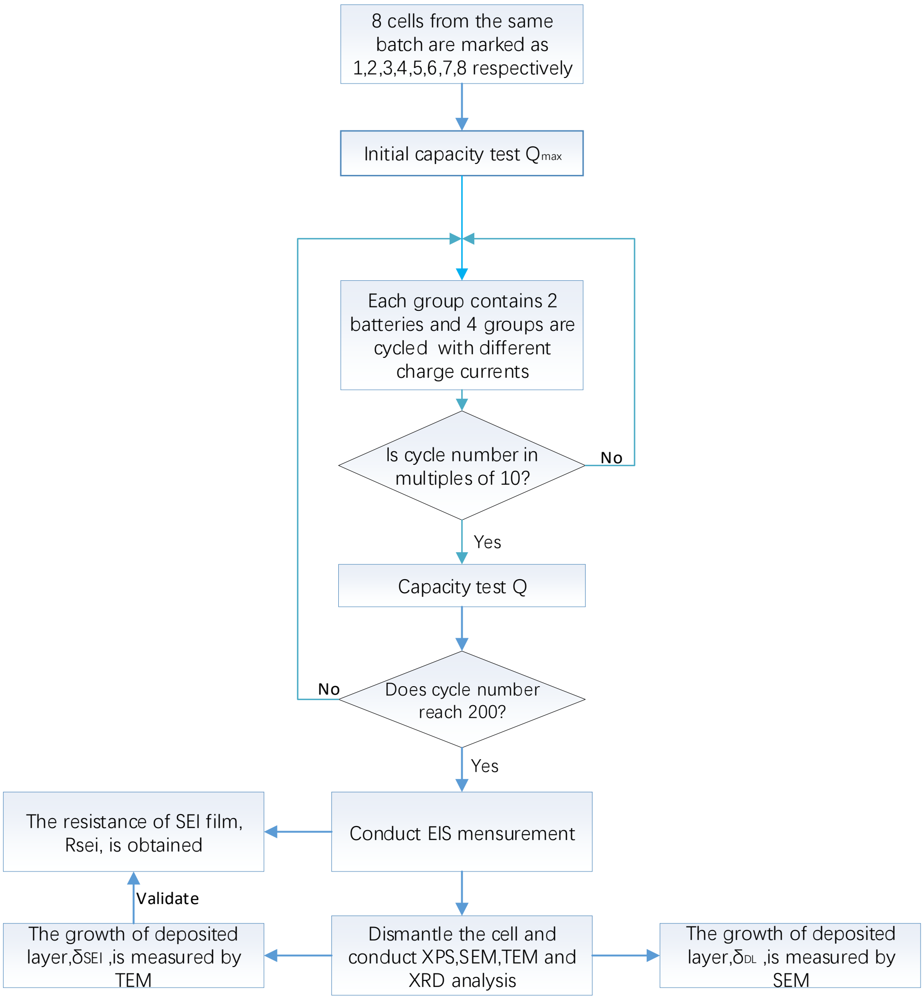

Figure 3. Flow chart of experiment.

Before disassembling, the cells are discharged full. Then the cells are opened up and the jellyrolls are rolled up in a glove box filled with argon. For post-mortem observation, small samples are taken at different positions of the jellyroll. Both the positive and negative electrodes are investigated using the scanning electron microscopy (SEM) and transmission electron microscope (TEM). The surface components of graphite electrodes are analyzed with the X-ray spectroscopy (XPS) and X-ray diffraction (XRD). The procedures of testing are summarized in Fig.3.

4. EXPERIMENTAL RESULTS

4.1. Capacity fade and resistance of SEI

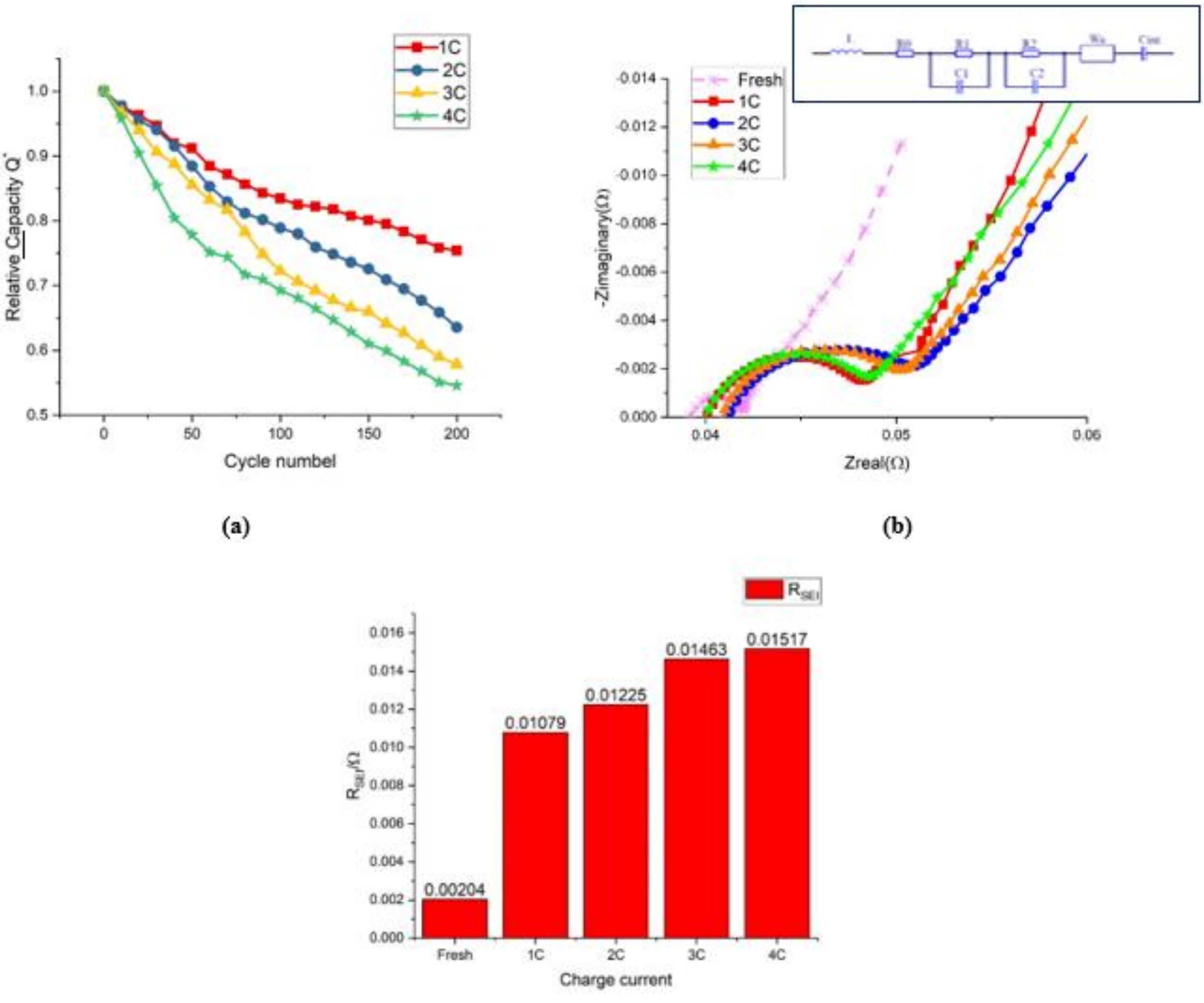

(a) (b)

(c)

Figure 4. (a) Capacity normalized to initial value over cycle number. (b) impedance spectra of cell at different cycling conditions and equivalent circuit network used to evaluate the impedance spectra. (c) resistance of the fresh cell and aged cells after 200 cycles.

The side reactions resulting in the formation of SEI is regarded as the dominant aging factor in most graphite-based lithium-ion batteries during cycling, which leads to capacity decline (due to loss of active lithium ions) [4,16,28-31]. In order to develop and parameterize an aging model, the aging behavior of capacity loss Q_{side} is measured in this work for different cycling conditions. The dimensionless relative capacity, Q^* is defined as $Q^* = \frac{Q_{fresh}}{Q_{aged}} = \frac{Q_{fresh}}{Q_{fresh} - Q_{side}}$ for comparison and shown in Fig. 4a. As illustrated in Fig. 4a, the 4C charge current condition causes the worst capacity fade. At the beginning of cycling, considerable capacity decay occurs due to the stabilization of SEI. After certain number of cycles, the slope of capacity decay becomes small resulting from irreversible side reactions which leads to the slow growth of SEI [32-35]. When the cycle number reaches 200, the relative capacity, Q^*, for 1 C,2 C,3 C and 4 C charge rates is 77.2%, 70.4%, 66.8% and 64.8%, respectively.

Fig. 4b shows the evolution of full-cell impedance spectra. The intercept with real axis is usually dominated by ohm resistances like resistance of current collector and electrolyte. The mid-frequency semi-circle enlarges, accounting for the increase of SEI resistance. To analyze these tendencies in detail, an equivalent circuit network model is used as shown in Fig.4b. The inductance describes the inductive part of the spectra, the serial resistance the intercept with the real axis. The first R_1&C_1 pair accounts for the mid-frequency semi-circle, resulting from the resistance of SEI and capacitance. The second R_2&C_2 pair is used to describe the diffusion behavior. W_a and C_{int} denote Warburg impedance and intercalation capacitance, respectively [16,22,36-38]. The resistance of SEI is drawn in Fig.4d by using the EIS-fitting (EIS-ECM) method. As shown in Fig.4c, when the cycle numbers are the same, the resistance of SEI (R_{SEI}) under the 4C charge current condition is nearly five times larger than that of fresh cells.

4.2. Visual and morphological observations

Fig.5a shows photographs of the anodes from a newly opened cell whose surface is homogenous and smooth. The cycled graphite electrodes have a striking variation in appearance along the jellyroll. The exfoliation of graphite from the copper current collector can be seen in Fig.5b, indicating that there is a loss of adhesion between carbon particles and between carbon particles and the current copper collector on the anode. While unrolling the innermost parts of the jellyroll, the white deposited layer is obvious in Figs.5c and 5d showing that the side reactions are more severe close to the core. This results from a high concentration gradient near the core which is the most conductive to the side reactions [16-17,28-29,39]. During the ion diffusion process, inhomogeneous distribution of Li-ions in an electrode particle causes inhomogeneous localized volume expansions, which induces mechanical stress. When stress exceeds certain limits, the electrode would experience material failure, associated with cracking or fracture [8,40-41].

(a)

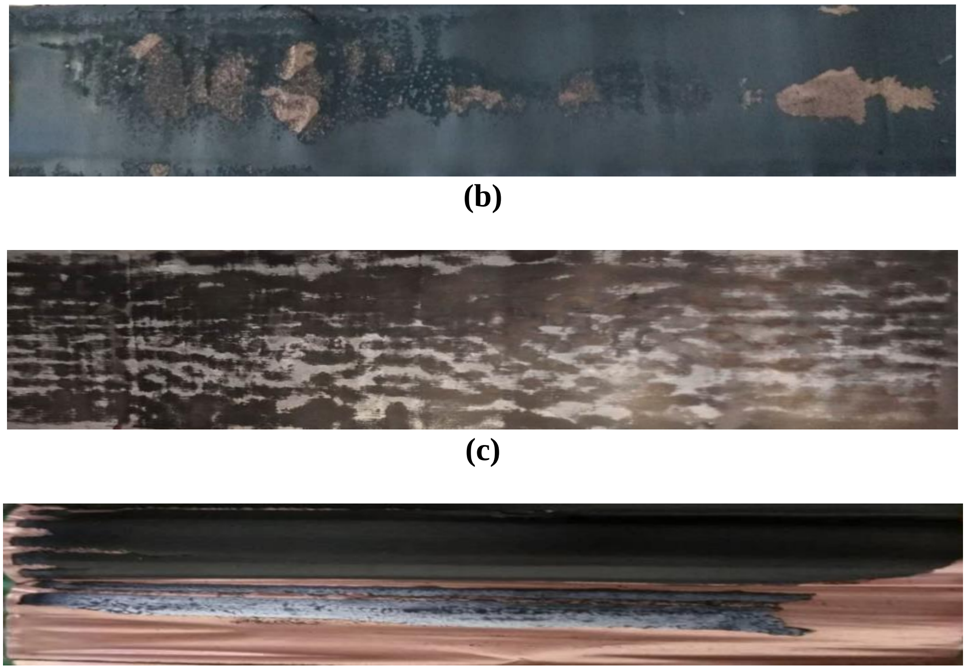

(b)

(c)

(d)

Figure 5. (a) Photograph of fresh negative electrode. (b) aged cells with graphite detachment. (c) aged cells with white deposited layer . (d) inner core of aged cells.

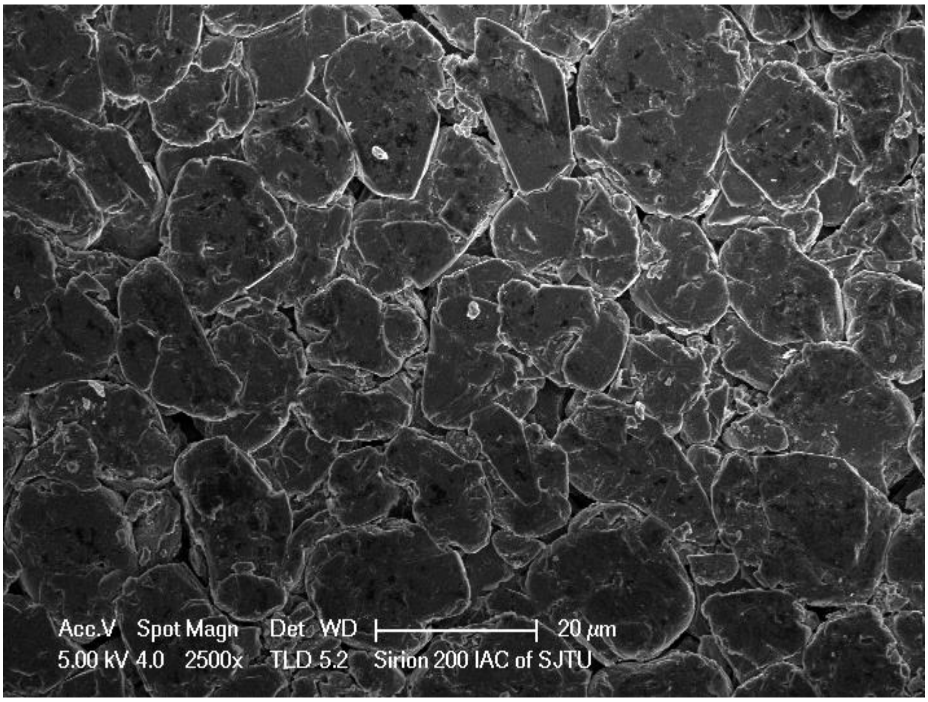

(a)

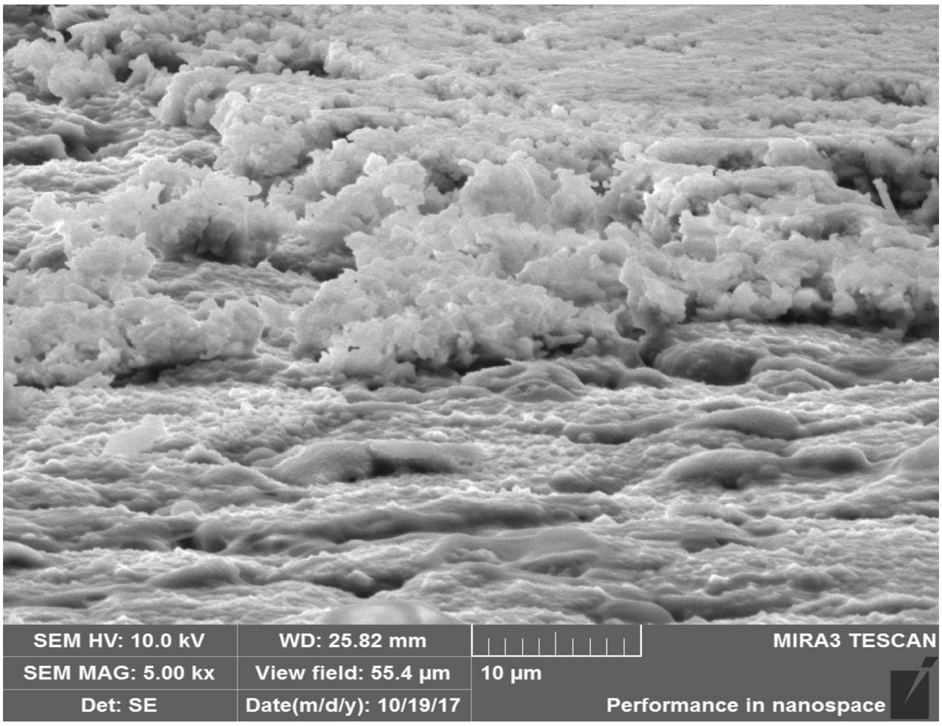
SEM HV: 10.0 kV
WD: 25.82 mm
MIRA3 TESCAN
SEM MAG: 5.00 kx
View field: 55.4 µm
10 µm
Det: SE
Date(m/d/y): 10/19/17
Performance in nanospace

(b)

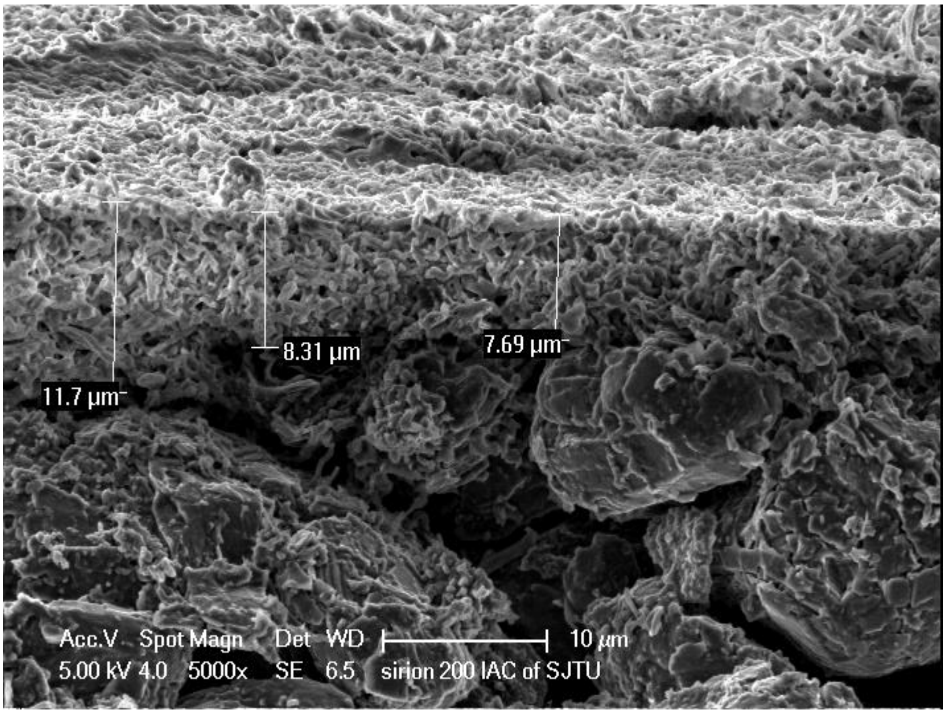
8.31 µm
7.69 µm
11.7 µm
Acc.V Spot Magn Det WD
5.00 kV 4.0 5000x SE 6.5
10 µm
sirion 200 IAC of SJTU

(c)

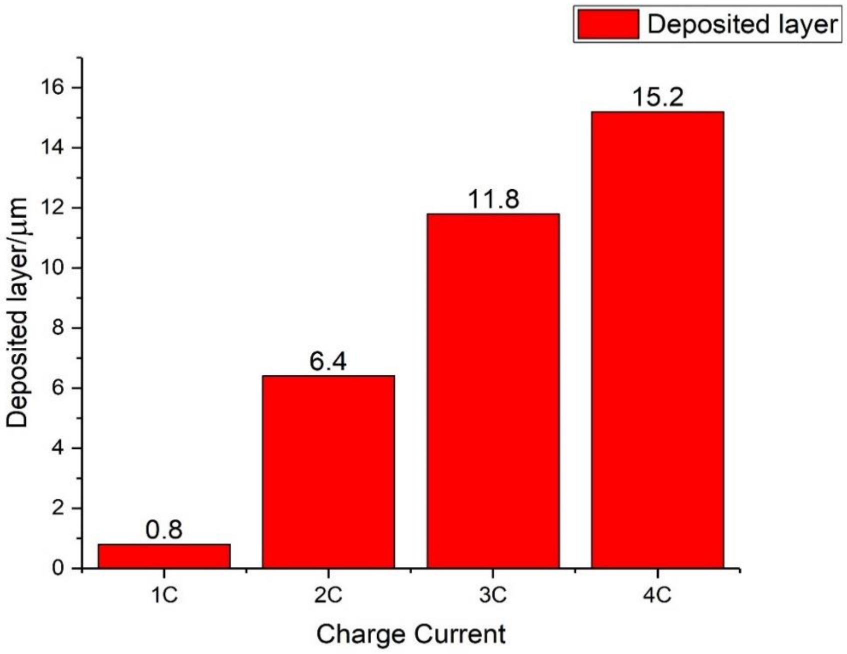

(d)

Figure 6. (a) SEM image of fresh graphite negative electrode. (b) deposited layer of aged cells. (c) cross-section view of deposited layer. (d) thickness of deposited layer under different charge currents.

A more detailed morphological comparison of the different electrodes using SEM is depicted in Fig.6. The fresh negative composite electrodes are rather uniformly thick consisting of Nano-sized particles as displayed in Fig.6a. In contrast, the aged anode surface depicted in Fig.6b has a thick deposited layer. The cross-section of a degraded anode is revealed in Fig.6c to measure the thickness of deposited layer. The single sample is measured three times to obtain an average value of thickness of the deposited layer. The thickness of deposited layer is illustrated in Fig.6d.

4.3. SEI thickness and composition analysis

For a detailed characterization of the surface film content and to measure the SEI thickness, the TEM, XPS and XRD are performed on the negative electrodes. The sample is prepared by cryosection before being loaded on the TEM holder. The TEM image of SEI is presented in Figs.7a and 7b. The single sample is measured three times to obtain an average value of SEI thickness. Fig.7c gives the results of SEI measurement.

The XPS is also employed to investigate the presence of Li on the SEI layer of the graphite anode as shown in Figs.7d and 7e. The binding energy for Li1s, C1s, and O1s (stand for the photoelectron peaks of Li, C and O, respectively) are summarized in Table 3, including those characterized in Li_2CO_3 in Ref [52-53].

Comparison in the Table 3 shows that the binding energies measured for Li1s, C1s, and O1s correspond to those found in the two standard Li_2CO_3 studies indicating that SEI layer is mainly composed of Li_2CO_3. The XRD spectra of fresh and aged anode electrodes in Fig.7f also show no phase change or new phase formation in the active materials of anode and cathode. This could be caused by the electronic isolation of Li_2CO_3 film in the deposits. The deposits could completely isolate certain anode particles and active materials from further chemical reactions. Therefore, there would be no more phase change in both two electrodes [50-51].

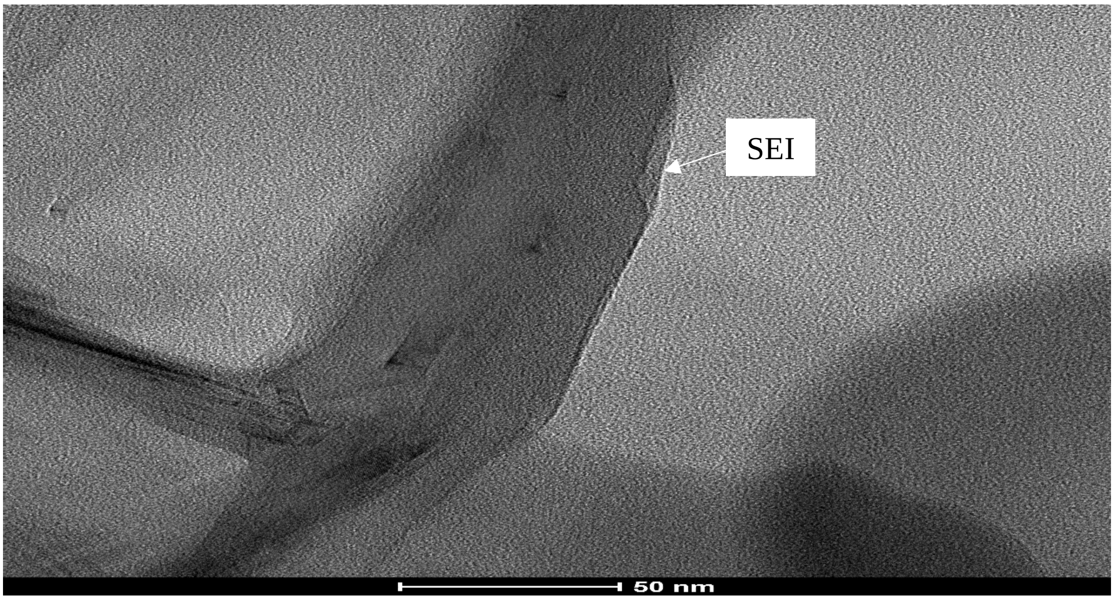

(a)

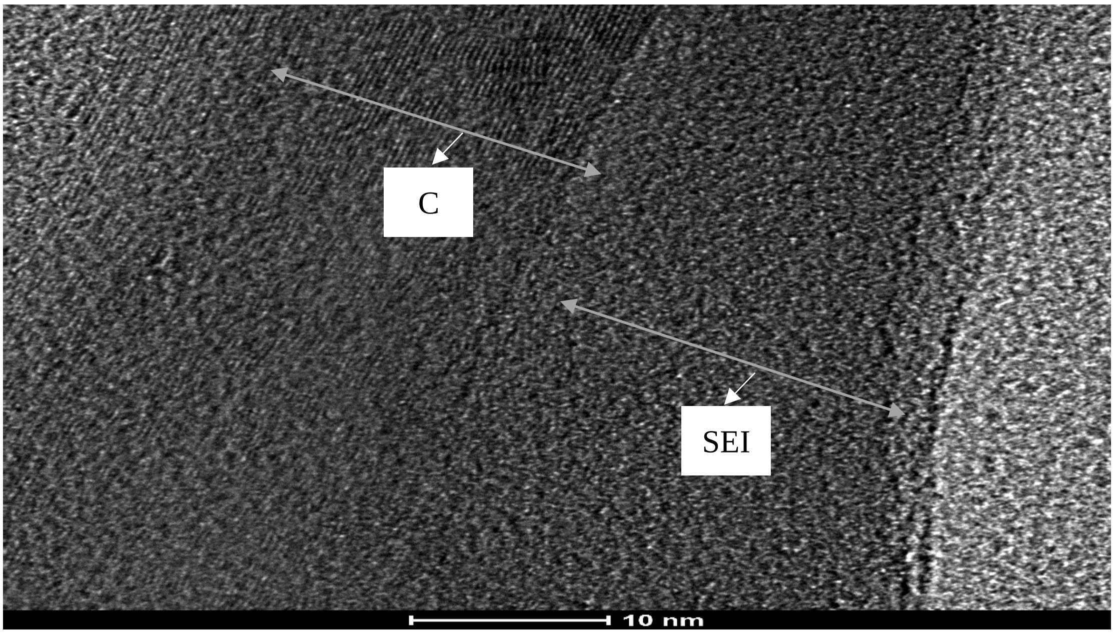

(b)

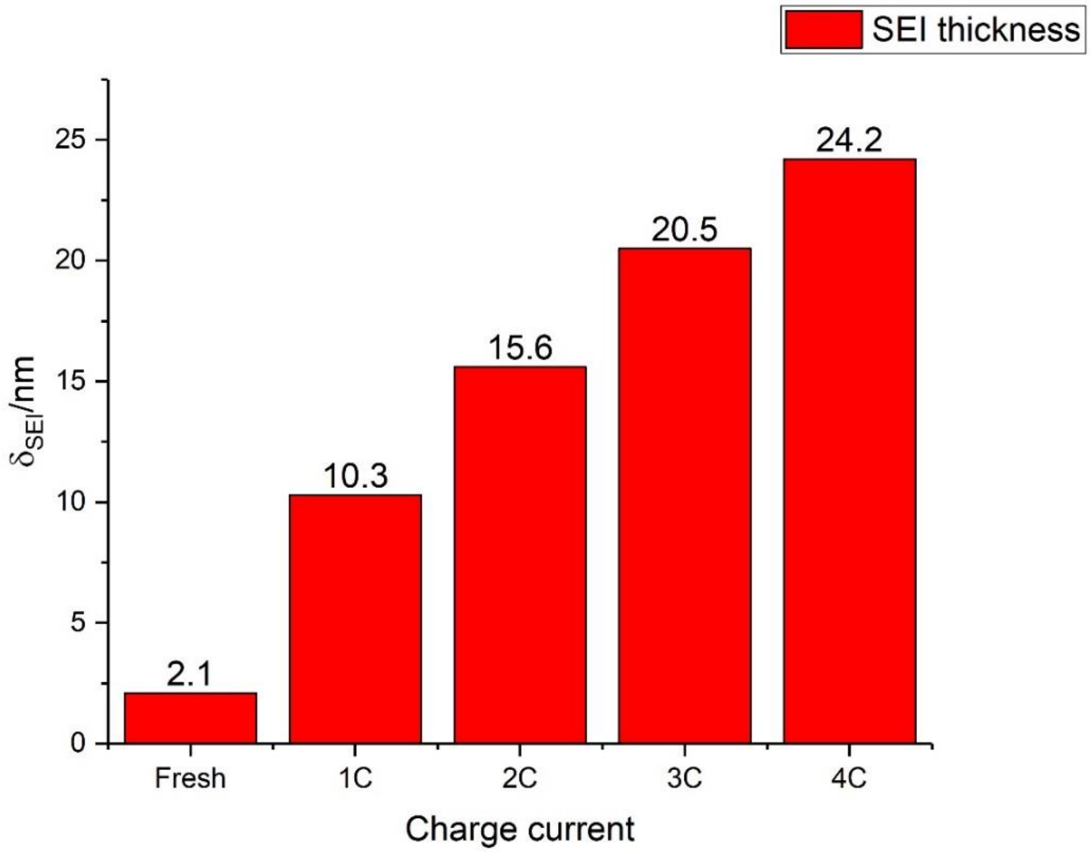
SEI thickness
δ_{SEI}/nm
0
5
10
15
20
25
2.1
10.3
15.6
20.5
24.2
Fresh
1C
2C
3C
4C
Charge current

(c)

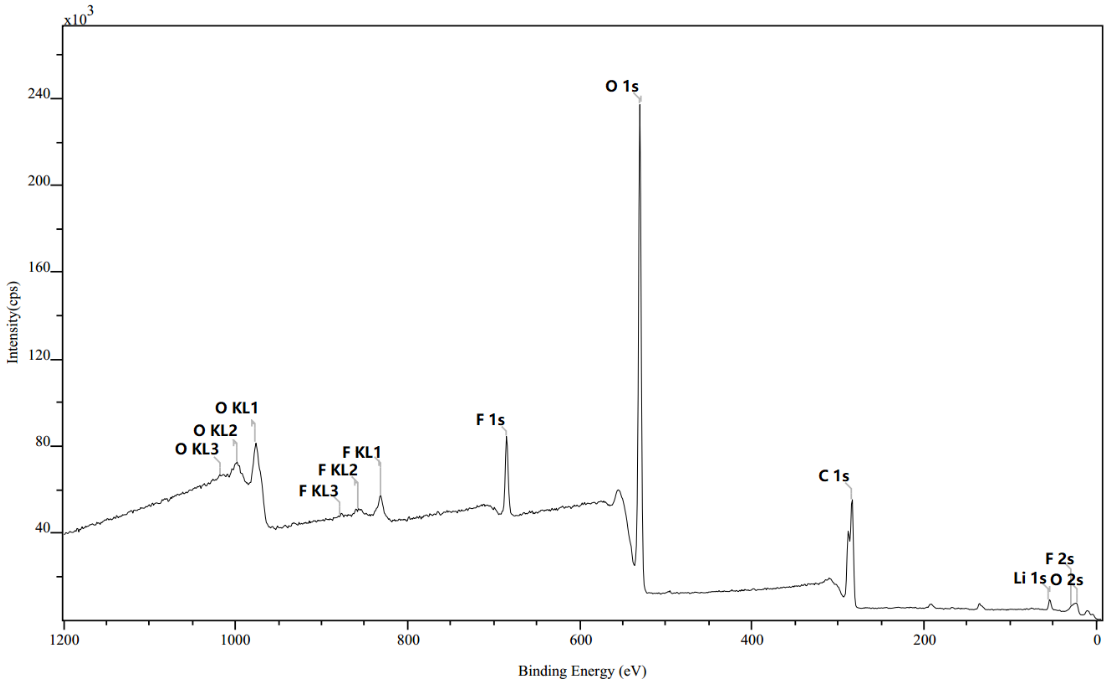
x10^3
240
200
160
120
80
40
Intensity(cps)
O 1s
O KL1
O KL2
O KL3
F 1s
F KL1
F KL2
F KL3
C 1s
F 2s
Li 1s
O 2s
1200
1000
800
600
400
200
0
Binding Energy (eV)

(d)

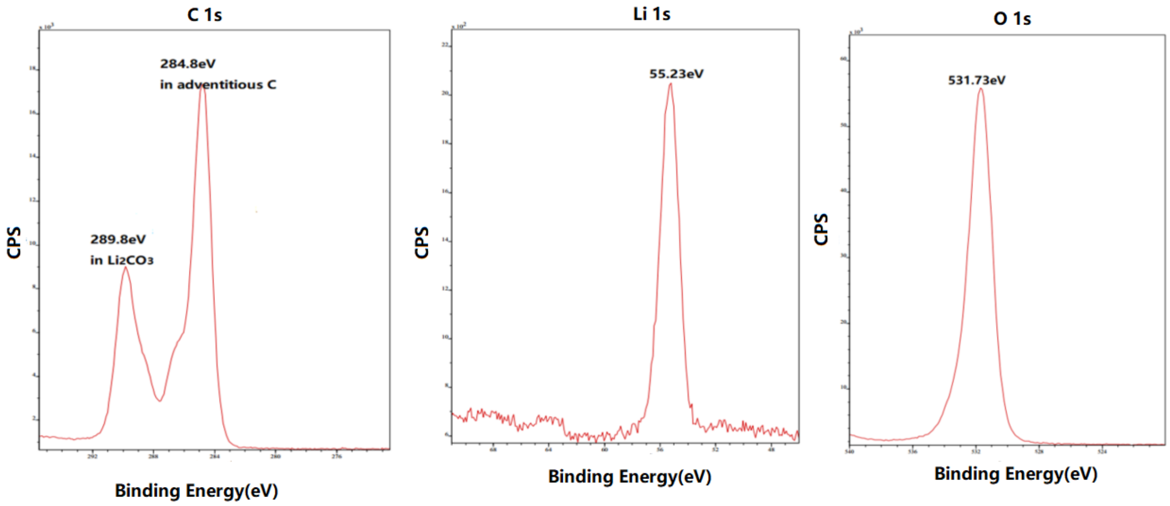

(e)

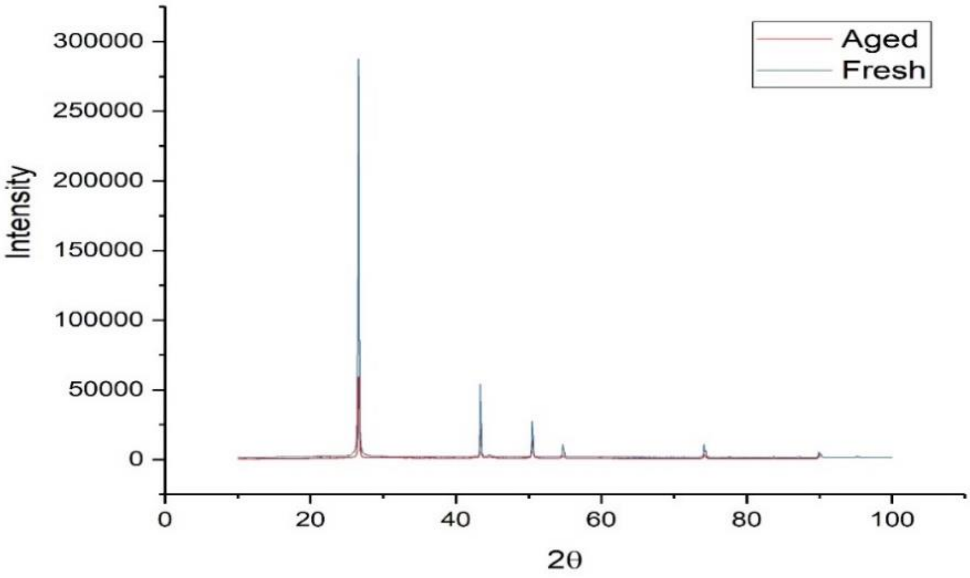

(f)

Figure 7. (a) TEM micrograph of SEI. (b) Magnified TEM image of (a). (c) Thickness of SEI measured from TEM micrographs of aged anode electrode after 200 cycles. (d)XPS spectra for aged anode. (e)Zoomed in XPS spectra. (f) XRD analysis of anode active material.

Table 3. Binding energies (eV) for Li_2CO_3 :

Investigator	C1s	Li1s	O1s
Our work	289.8	55.23	531.73
Reference in [52]	289.55	55.12	531.40

5. SIMULATION RESULT AND MODEL VALIDATION

The software COMSOL and MATLAB/Simulink are used to simulate the models based on the diagram in Fig.2. The COMSOL has been commonly regarded as a mature and effective software for electrochemical simulation [23,42]. Thus, the results by COMSOL are considered as a benchmark for comparison accordingly. The main parameters in Table 2 are utilized.

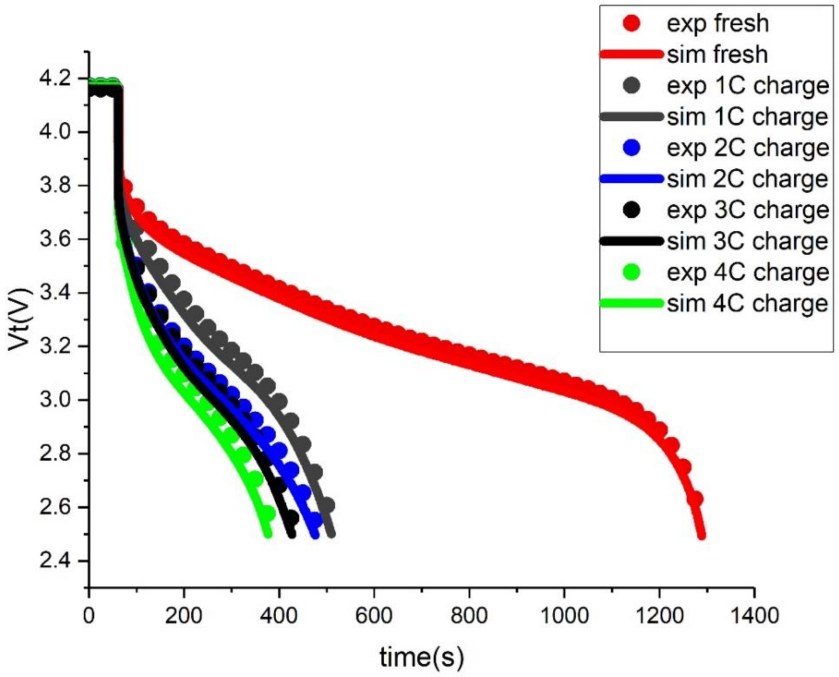

(a)

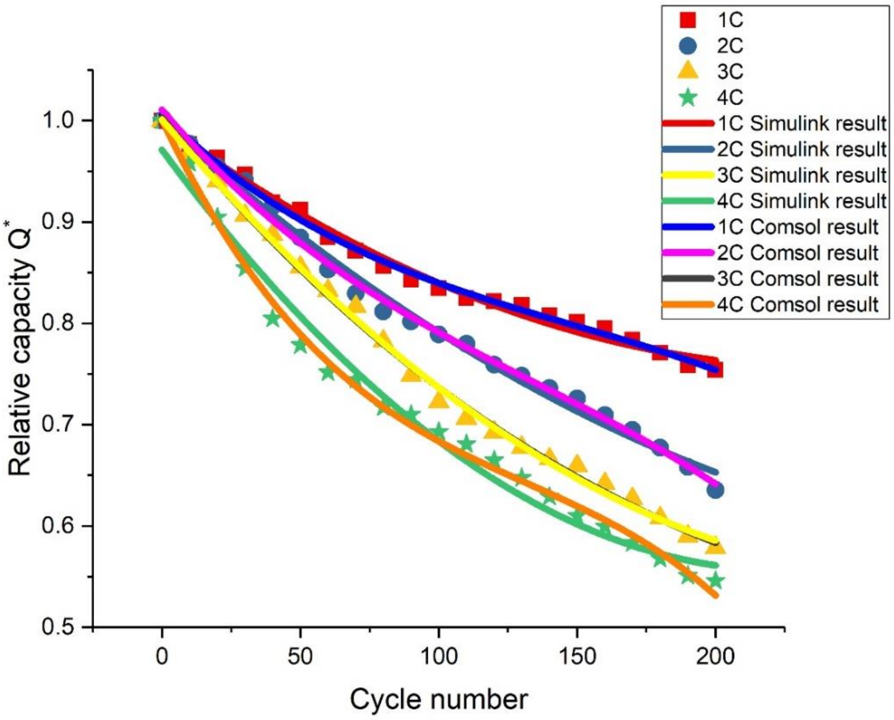

(b)

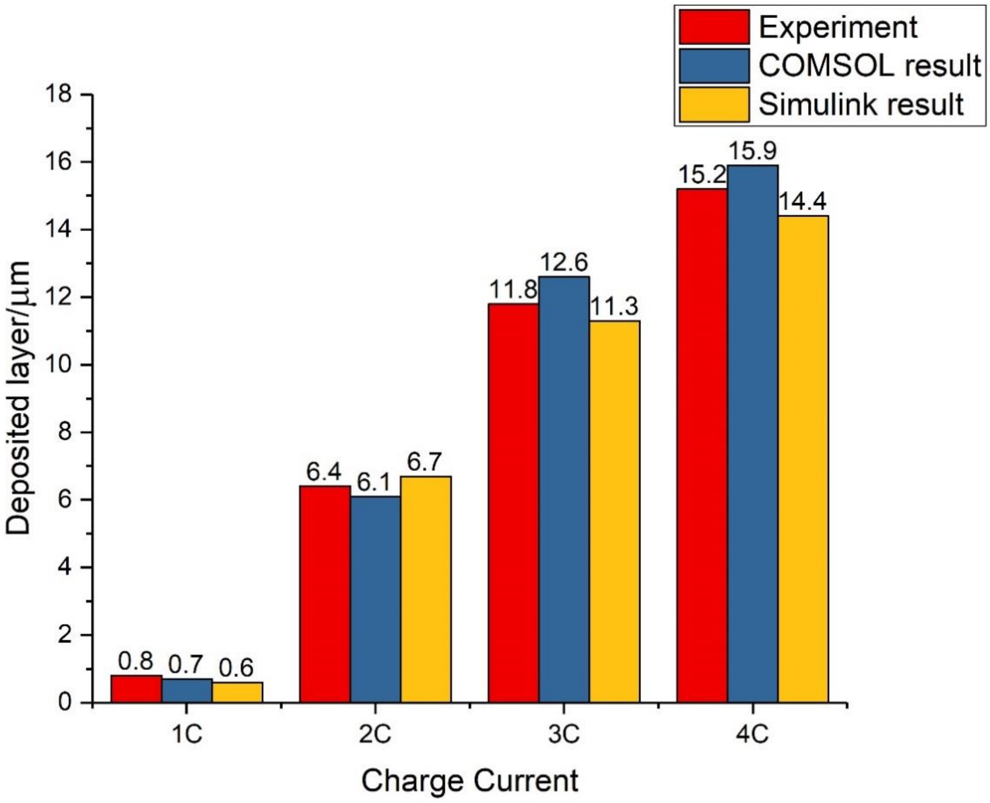
Experiment
COMSOL result
Simulink result
Deposited layer/μm
0
2
4
6
8
10
12
14
16
18
0.8
0.7
0.6
6.4
6.1
6.7
11.8
12.6
11.3
15.2
15.9
14.4
1C
2C
3C
4C
Charge Current

(c)

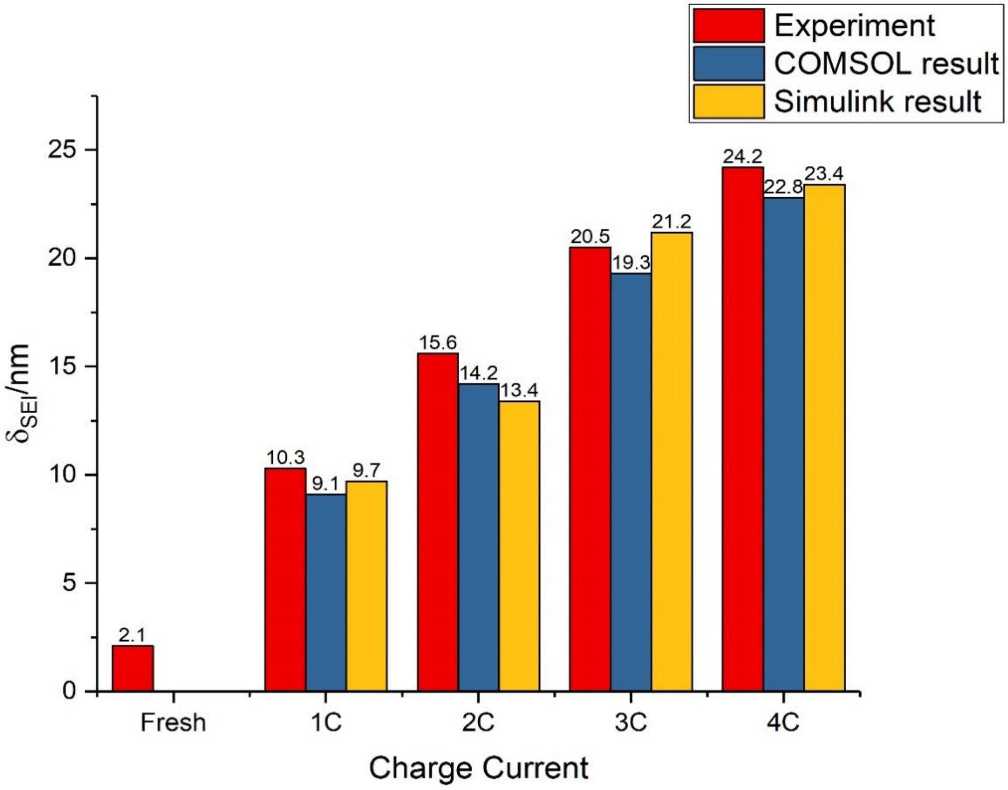
Experiment
COMSOL result
Simulink result
δ_{SEI}/nm
0
5
10
15
20
25
2.1
10.3
9.1
9.7
15.6
14.2
13.4
20.5
19.3
21.2
24.2
22.8
23.4
Fresh
1C
2C
3C
4C
Charge Current

(d)

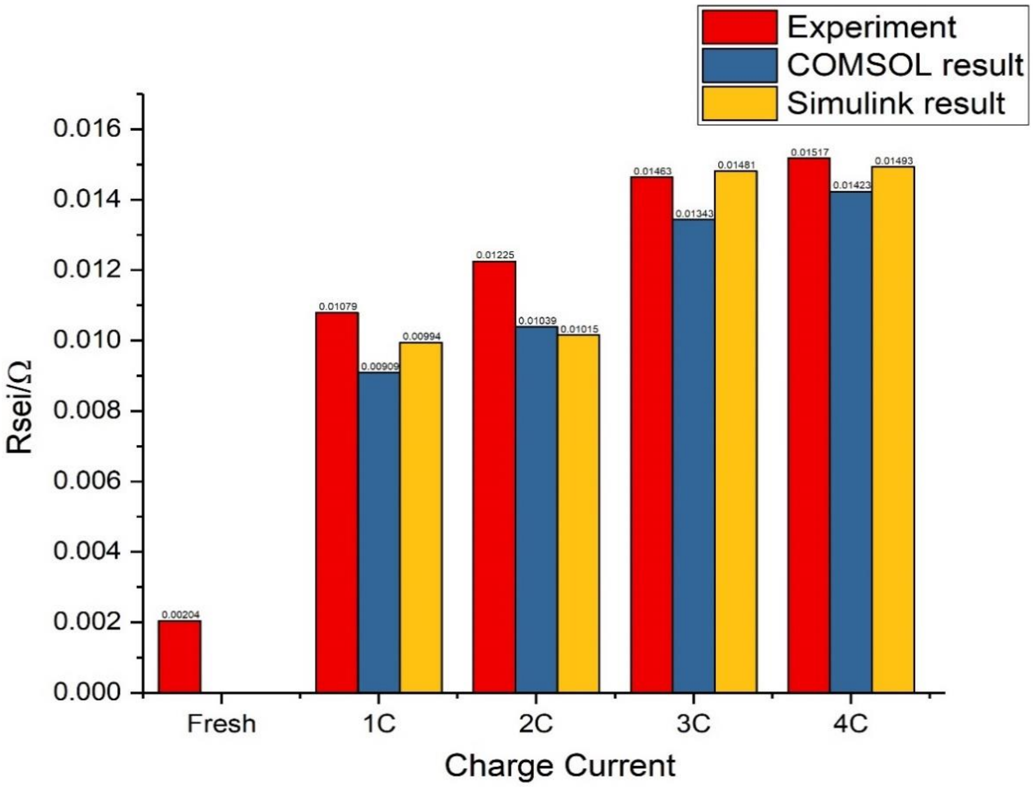

(e)

Figure 8. (a)3C discharge curve at 200 cycles under different charge C-rates. (b)simulation results of capacity fade. (c)simulation results of deposited layer thickness. (d)simulation results of SEI thickness. (e)simulation results of SEI resistance.

The simulation condition corresponds to cycling experiments. The models in COMSOL and Simulink are simulated with 1C, 2C, 3C and 4C charge rates and 3C discharge rate, respectively. Simulated and experimental discharge characteristics of the fresh and aged cells after 200 cycles as a function of charge C-rates are plotted in Fig.8a, where the discharge rate is 3C. The simulation results of three degradation representatives, capacity fade caused by side reaction, thickness of deposited layer and thickness of SEI, and resistance of SEI are listed in Figs.8b-8e respectively.

As is shown in Fig.8a, after considerable charge/discharge cycles, the discharge time of cells becomes shorter because of the faded capacity. In addition, the simulated discharge curve almost superposes the experimental values, which proves that the physics-based model still has a good precision in predicting current response after 200 cycles. This performance is superior to many other kinds of battery aging models such as durability model based [33,43]and parameter identification model based [48-49]. For capacity fade in Fig.8b, when the charge C-rates become larger, the capacity fade slightly increases. This might be caused by the intensive mechanical stress inside the particles, which potentially damages the battery structure [44-45]. In addition, the Li ions are much easier to accumulate on the anode surface under hash currents, which has more tendency to have side reactions [46-47]. The SEM measurement of deposited layer is compared with simulation in Fig.8c. The simulated SEI thickness and resistance is validated by TEM and EIS results in Fig.8d-8e, respectively.

From these figures, we can obviously see that the proposed improved electrochemical aging model fits the COMSOL model (considered as a benchmark) and follows the experimental data well within the maximum estimation error (<5%).

6. CONCLUSION

In this paper, a novel electrochemical aging model considering side reactions for lithium-ion batteries is proposed combined with the transfer-function type of the P2D model. The transfer function with the degradation parameter versus input currents is obtained on basis of mathematical schemes including the Laplace transform, inverse Laplace transform and Pade approximation. To validate the model, commercial Li-ion 18650 cells are used to be cycled under different conditions and opened for post-mortem analysis. Numerical and experimental analysis have highlighted on the mechanisms of capacity fade and power fade as well as their dependencies on different operating conditions. The key findings are summarized as below: First, Loss of ions and electrolyte and other aging phenomenon is the long-term impact of side reactions. In addition, charging at high C-rate process significantly increases the aging rate and causes more degradation. Second, From the simulated and experimental results, it can be verified that the proposed aging model with proper aging representatives could reflect the battery interior mechanism and quantify battery degradation severity, which makes it suitable for accurately evaluating the battery aging procedure.

ACKNOWLEDGEMENT

This work is supported by the National Natural Science Foundation of China (Grant No. 51677118).

NOMENCLATURE

A	sandwich area of the cell(m^2)	R	universal gas constant (8.3143j $mol^{-1}k^{-1}$) or resistance
δ_-	Thickness of negative electrode(m)	F	farady constant(96487c mol^{-1})
$\boldsymbol{t_+^0}$	cation transference number	L	length between cu collector and al collector(m)
Rs	paticle radius of active material(m)	ε_s	volume fraction of solid phase
$a_{s,i}$	specific surface area of electrode(m^{-1})	ε_e	volume fraction of liquid phase
D_s	diffusion coefficient in the solid phase(m^2s^{-1})	D_e	diffusion coefficient in the liquid phase(m^2s^{-1})

c_s	lithium concentration in the solid phase(mol m^{-3})	c_e	lithium concentration in the liquid phase (mol m^{-3})
k	reaction rate constant of electrode (mol$^{-1/2}$m$^{5/2}$ s^{-1})	κ	ionic conductivity (s m^{-1})
α_a	transfer coefficient for anode reaction	α_c	transfer coefficient for cathode reaction
ф	potential in the electrolyte	Q	capacity
V_{SEI}	molar volume of SEI	i_0	exchange current density (Am^{-2})
j_{side}	current density of side reactions	j_{int}	current density of intercalation reactions
R_{SEI}	resistance of SEI	δ_{SEI}	thickness of SEI(m)
δ_{DL}	thickness of deposited layer(m)	η	overpotential on the electrode

References

1. J. Marcicki, M. Canova, A.T. Conlisk and G.Rizzoni, *J. Power Sources*, 237 (2013) 310.
2. H. Wu, S. Yuan, X. Zhang, C. Yin and X.Ma, *J. Power Sources*, 287 (2015) 108.
3. X. G. Yang, Y. Leng, G. Zhang, S. Ge and C-Y. Wang, *J. Power Sources*, 360 (2017) 28.
4. X. Zhou, D. S, Bernstein, J. L . Stein and T. Ersal, *J. Dyn. Syst. Meas. Control-Trans. ASME.*, 139 (2017) 15.
5. J. Vetter, P. Novák, M. R. Wagner, C. Veit, K.-C. Möller, J.O. Besenhard, M.Winter,M. Wohlfahrt-Mehrens and C. Vogler, *J. Power Sources*,147 (2005) 269.
6. E. Sarasketa-Zabala, I. Gandiaga, L. Rodriguez-Martinez and I. Villarreal, *J. Power Sources*, 272 (2014) 45.
7. G. Ning, R.E. White and B. N. Popov , *Electrochimica Acta*, 51 (2006) 2012.
8. R. Fu, S. -Y. Choe, V. Agubra and J. Fergus, *J. Power Sources*, 278 (2015) 506.
9. P. Verma, P. Maire and P. Novák, *Electrochimica Acta*, 55 (2010) 6332.
10. R. Fu, S. -Y. Choe, V. Agubra and J. Fergus, *J.Power Sources*, 261(2014)120.
11. H. Bryngelsson, M. Stjerndahl and T. Gustafsson, *J. Power Sources*,174 (2007) 970.
12. J. Amanor-Boadu, M.A. Guiseppi-Elie and E. Sanchez-Sinencio, *IEEE Trans. Indus Electron.*, 65 (2018) 8982.
13. H. Jannesari, M.D. Emami and C. Ziegler, *J. Power Sources*, 196 (2011) 9654.
14. V. Etacheri, R. Marom, R. Elazari, G. Salitra and D. Aurbach, *Energy & Environmental Science*, 4 (2011) 1310.
15. V. Agubra and J. Fergus, *J. Materials (Basel)*, 6 (2013) 1310.

16. M. Klett, R. Eriksson, J. Groot, P. Svens, K.C. Högström, R.W. Lindström, H. Berg, T. Gustafson, G. Lindbergh and K. Edström, *J. Power Sources*, 257 (2014) 126.
17. V.A. Agubra, J. Fergus, R. Fu and S.-Y. Choe, *J. Power Sources*, 270 (2014) 213.
18. M. Doyle and J. Newman, *J. Electrochem Soc.*, *143* (1996) 1890.
19. T.R. Tanim and C.D. Rahn, *J, Power Sources*, 294 (2015) 239.
20. G. Liu,M. Ouyang, L. Lu, J. Li and X. Han, *J. Therm.Anal.Calorim.*, 116 (2014) 1001.
21. X. Jin, A. Vora, V. Hoshing, T. Saha, G. Shaver, R.E García, O. Wasynczuk and S. Varigonda, *J. Power Sources*, 342 (2017) 750.
22. G. Sikha, B. Popov and N.R. White, *J. Electrochem Soc.*, 151 (2004) A1104.
23. X. Zhang, J. Lu, S. Yuan, J. Yang and X. Zhou, *J. Power Sources*, 345 (2017) 21.
24. S. Yuan, L. Jiang, C. Yin, H. Wu and X. Zhang, *J. Power Sources*, 352 (2017) 258.
25. S. Yuan, L. Jiang, C. Yin, H. Wu and X. Zhang, *J. Power Sources*,352 (2017) 245.
26. R. Fu, M. Xiao and S-Y. Choe, *J. Power Sources*, 224 (2013) 211.
27. T.R. Ashwin, Y.M Chung and J. Wang, *J. Power Sources*, 328 (2016) 586.
28. T. Yoshid, M. Takahashi, M. Satoshi and J. Yamakic , *J. Electrochem Soc.*, 153 (2006) A576.
29. S. Phul, A. Deshpande and B. Krishnamurthy, *Electrochimica Acta*, 164 (2015) 281.
30. J. Zhu, K. Zeng and L. Lu, *Electrochimica Acta*, 68 (2012) 52.
31. K. Zaghib, M. Dontigny, A. Guerfi and P. Rodrigues, *J. Power Sources*, 6 (2011) 3949.
32. K. Smith and C-Y. Wang, *J. Power Sources*,161 (2006) 628.
33. P. Ramadass, B. Haran, M.P. Gomadam, R. White, and B. N. Popov, *J. Electrochem Soc.*, 151 (2004) A196.
34. W. Appiah, A. Park, J. Byun, S. Ryou, M.H. Lee and Y. M, *J.Electrochem Soc.,163* (2016) A2757.
35. H. Ekstrom, G. Lindbergh, *J. Electrochem Soc.*, 162 (2015) A1003.
36. X. Lin, H.E. Perez, S. Mohan, S. Siegel, J.B. Stefanopoulou, A.G. Ding, Y. Castanier and M. P, *J. Power Sources*, 257 (2014) 1.
37. J. Illig, J.P. Schmidt, M. Weiss, A. Weber and E. Ivers-Tiffée, *J. Power Sources*, 239 (2013) 670.
38. K. Amine, J. Liu and I. Belharouak, *Electrochem. Commun*., 7 (2005) 669.
39. M. Koltypin, D.Aurbach, L. Nazar and B. Ellis, *J. Power Sources*, 174 (2007) 1241.
40. J. Christensen and J. Newman, *J. Solid State Chem*., 10 (2006) 293.
41. J. Christensen and J. Newman, *J. Electrochem Soc*., 156 (2006) A1019.
42. L.C. White and R. E, *J. Power Sources.*, 196 (2011) 5985.
43. M. Safari, M. Morcrette and A. Teyssot, *J. Electrochem Soc.*, 156 (2009) A145.
44. J. Groot, J. Swierczynski, M. Stan, A. I. Kær and S. K, *J. Power Sources*, 286 (2015) 475.
45. Y. Gao, J. Jiang, C. Zhang, W. Zhang and Z. Jiang, *J. Power Sources*,356 (2017) 103.
46. B. K. Purushothaman. P.W. Morrison and U. Landauz. *J. Electrochem Soc.*, 152 (2005) J33.
47. B. K. Purushothaman and U. Landauz, *J. Electrochem Soc*., 153 (2006) A533.
48. L.P. Gregory, *J. Power Sources*, 134 (2004) 277.
49. L. Seongjun, K. Jonghoon, L. Jaemoon and B.H. Cho, *J. Power Sources*, (185) (2008) 1367
50. D. Aurbach, D.L. Mikhail and E. Levi, *J. Phys. Chem.*,101 (1997) 2195.
51. S. Shi, P. Lu, Z. Liu, Y. Qi, L. Hector, H. Li and S. Harris, *J. Am. Chem. Sci.*, 134 (2012) 15476.
52. S. Contarni and J.W. Rabalais, *J. Electron Spectrosc. Relat. Phenom*., 35 (1985) 191.
53. J.P. Contour, A. Salesse, M. Froment, M. Garreau, J. Thevenin and D. Warin, *J. Microsc. Spectrosc. Electron.*, 4 (1979) 483.